Journal of Nuclear Materials 393 (2009) 67–76

Contents lists available at ScienceDirect

Journal of Nuclear Materials

journal homepage: www.elsevier.com/locate/jnucmat

# Elastic and plastic properties of $\beta_{Zr}$ at room temperature

S. Cai [a], M.R. Daymond [a,*], A.K. Khan [a], R.A. Holt [a], E.C. Oliver [b]

[a] Dept. of Mechanical and Materials Engineering, Queen's University, Nicol Hall, 60 Union Street, Kingston, Ontario, Canada K7L 3N6
[b] ISIS, Rutherford Appleton Lab., Didcot, OX11 0QX, UK

ARTICLE INFO

*Article history:*
Received 18 August 2008
Accepted 14 May 2009

ABSTRACT

Room temperature elastic and plastic properties of a single phase $\beta_{Zr}$ have been studied by *in-situ* neutron diffraction compression testing. The measured macroscopic Young's modulus is ~60 GPa and the yield strength is ~500 MPa. Dislocation slip is the major mode of plastic deformation. An Elasto-Plastic Self-Consistent (EPSC) model was used to interpret the experimental results and was shown to be effective in extracting the single crystal properties from the polycrystalline data. The single crystal elastic constants of the β-phase are determined as: $C_{11} = 145.9 \pm 2.6$ GPa, $C_{12} = 117.4 \pm 2.5$ GPa and $C_{44} = 29.8 \pm 0.2$ GPa. The calculated elastic modulus of $\langle 1\,0\,0\rangle$, $\langle 1\,1\,0\rangle$, $\langle 1\,1\,1\rangle$, $\langle 2\,1\,1\rangle$ and $\langle 3\,1\,0\rangle$ directions was ~41.2, 66.2, 82.9, 66.2 and 47.7 GPa, respectively. Pencil glide on the {110}, {112} and {123} planes was used in the EPSC model and gave a good simulation to the early part of the plastic deformation. The average β-phase strain is best represented by the peak average method, while in cases where only a limited number of diffraction peaks are available, the {211} grain family is a good candidate for estimation of the average β-phase strain.

## 1. Introduction

Zr–2.5Nb has been of interest as the pressure tube material in CANDU and RBMK reactors [1]. It's deformation, especially the in-reactor deformation, has been extensively studied over the past 40 years. The effects of the major variables such as neutron flux, temperature, texture and residual stresses are broadly understood [2]. Like Ti–6Al–4V, it consists of an α-phase, which has a *hcp* crystal structure, and a minority β-phase, which has a *bcc* crystal structure. The deformation behavior of the material depends on the phase properties and the interactions between the two phases. In (α+β) dual phase Ti alloys, it has been found that the texture evolution strongly depends on the second phase [3] and phase interactions alter the deformation modes operating in each phase compared to those operating in their single phase state [4]. Similarly, the β-phase in Zr–2.5Nb was also noticed to affect the texture evolution of the dual phase system during annealing [5]. The study of Cheadle and Aldridge on a Zr–19%Nb alloy [6] implies that the extruded Zr–2.5Nb pressure tubes will harden during fabrication and operation due to the decomposition of $\beta_{Zr}$ into a mixture of *hcp* ω and Nb enriched $\beta_{Zr}$ phase. However, despite many years study on the deformation mechanism of Zr–2.5Nb [5,7], the contribution of the β-phase still remains poorly understood and the mechanical properties of $\beta_{Zr}$ at room temperature are still uncertain. Part of the reason is the small volume fraction of β-phase in Zr–2.5Nb, ~10% at room temperature. People have traditionally ignored its presence and have fitted single phase models to two phase experimental data [8,9]. In Ref. [10], the β-phase was reported to be softer compared to the α-phase in the Zr–2.5Nb pressure tube material and to accommodate most of the strain during deformation. The absence of texture development in the cold rolled Zr–2.5Nb was then attributed to the rigid body rotation of the α grains. However, our recent work suggests that the β-phase is actually stronger than the α-phase and yields at a higher macroscopic applied stress during uniaxial deformation [11]. Nishimura et al. [12] have studied three different plastic deformation modes in β-phase ZrNb alloys with different Nb contents at temperatures of 77 and 290 K: $\{332\}\langle 1\,1\,3\rangle$ twinning, $\{112\}\langle 1\,1\,1\rangle$ twinning and $\{112\}\langle 1\,1\,1\rangle$ slip, with the activity of the different modes found to be dependent on alloying. Like the β-phase of Ti [13], it is found that the presence of $\{332\}\langle 1\,1\,3\rangle$ twinning was related to the β- to ω-phase decomposition, with $\{112\}\langle 1\,1\,1\rangle$ twinning tending to be found only in the stable high Nb content alloys. The activity of dislocation slip systems in $\beta_{Zr}$ increases with increasing Nb content, to very high Nb contents (>50 wt%), at which point twinning activity starts to increase again. In this paper, we report room temperature deformation characteristics of 100% $\beta_{Zr}$. The single crystal elastic and plastic properties determined from the polycrystalline experimental data will help us to understand the role of the β-phase in the multiphase Zr–2.5Nb and will be useful in modeling the deformation behaviors of ZrNb alloys.

---

* Corresponding author.
*E-mail address:* daymond@me.queensu.ca (M.R. Daymond).

0022-3115/$ - see front matter © 2009 Elsevier B.V. All rights reserved.
doi:10.1016/j.jnucmat.2009.05.007

## 2. Materials and experimental method

The material used in this experiment, which is termed Zr–20%Nb, is an extruded bar that was made by Teledyne (now ATI) Wah Chang. The chemical composition is 19.3 wt% Nb, 1360 wppm O, 518 wppm Fe, 100 wppm C, balance Zr plus trace impurities. Quenching experiments were carried out to obtain 100% β-phase. Several pieces of this material were cut from the bar for heat treatment, and then standard compression samples were cut from the heat treated bar. For compression samples aligned transverse to the original bar axis, the size of heat treated material was ~Ø50 × 15 mm. For compression samples aligned axial to the original bar direction, the heat treated material size is ~20 × 20 × 60 mm with the long direction parallel to the bar axial direction. The blocks were sealed in stainless steel foil bags, filled with argon, and then heated in an air furnace to 1000 °C for 15 min, furnace cooled to specified temperatures, then water quenched to room temperature. Based on the binary Zr–Nb phase diagram [14], 100% $\beta_{Zr}$ is expected at a temperature of ~630 °C. However, Fig. 1(a) shows that after quenching from this temperature, a significant number of α grains are still present. This is likely caused by α-phase stabilization due to the presence of O [15], and is in agreement with [16,48]. Near 100% β-phase could only be obtained at room temperature by quenching from temperatures above 800 °C (Fig. 1(b)). The etch pits in Fig. 1(b)) correspond to areas with small amounts of α-phase present (approximately 5 vol.% α-phase at each location, hence ≪1% by volume overall) while the rest of the sample is fully β-phase. For the current experiment, the quenching temperature used was ~830 °C, which produced an average grain size about 150 μm. Compression samples were cut

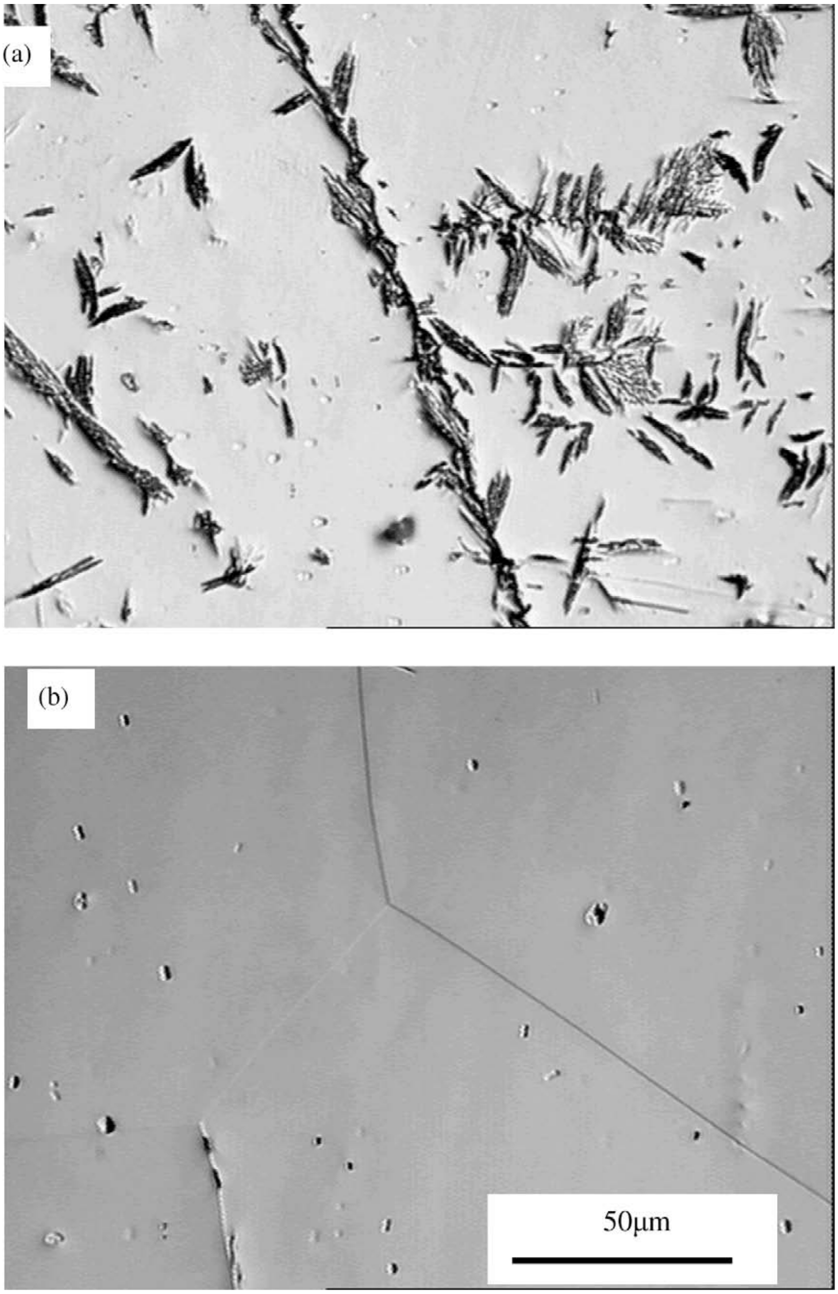

**Fig. 1.** Microstructure of the Zr–20%Nb quenched from: (a) 630 °C and (b) 800 °C after holding at 1000 °C for 15 min and furnace cool to the quench temperature. Dots in (b) are etch pits.

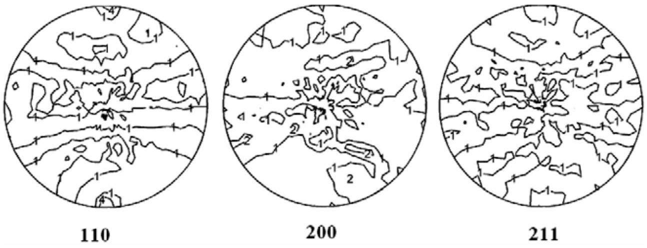

**Fig. 2.** Texture of the sample material, vertical is the bar axial direction, horizontal to center is the bar transverse direction.

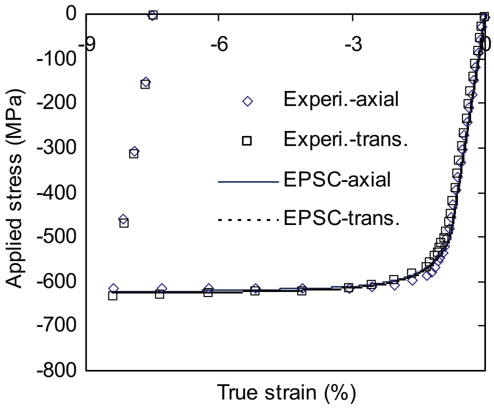

**Fig. 3.** Macroscopic mechanical properties of the single phase $\beta_{Zr}$. Dots are experimental data and lines represent the EPSC modeling results.

from the heat treated material with a size ~8 mm diameter × 20 mm long with the axis parallel to either the axial or radial direction of the bar. It should be noted that $\beta_{Zr}$ of this composition is a metastable phase at room temperature; upon annealing it will partially transform towards equilibrium $\alpha_{Zr}$ and *bcc* $\beta_{Nb}$ and hence consist of a mixture of a metastable *hcp* ω-phase and Nb enriched $\beta_{Zr}$ [6]. TEM on the material immediately after the heat treatment found no ω-phase to be present, however, TEM of the material after deformation tests (carried out approximately 3 months after the samples were made) showed a small quantity of ω-phase [16] (≪1% by volume) present. The ω-phase precipitates were highly distorted with strongly smeared diffraction patterns.

The texture of the heat treated material was measured at the E3 spectrometer at the National Research Universal (NRU) reactor at the AECL Chalk River Laboratory. Fig. 2 shows that the material has a weak texture with the ⟨1 1 0⟩ direction aligned with the bar axial and radial directions, showing a typical character of extrusion texture for a *bcc* material [17,18,19]. The {200} and {211} planes appear randomly orientated.

The compression tests were carried out on ENGIN-X at the ISIS pulsed neutron facility, Rutherford Appleton Laboratory. The loading axis was horizontal and at 45° to the horizontal incident beam. Two detector banks are set up horizontally and at angles ±90° to the incident beam, allowing simultaneous measurement of lattice strains in two directions, one parallel and one perpendicular to the applied load [20]. More details of the instrument can be found in [21]. A series of increasing uniaxial compressive loads were applied along the axial sample direction to produce a final true strain of ~8%. Strain was monitored on the samples using a clip gauge. The experiment was carried out under strain control; each time the sample was deformed to the desired strain and held for 30 s to allow for any stress relaxation, which was at most ~10% of the peak load for a step in the plastic regime. Data acquisition time was then around 10 min at each point. During the data acquisition period, stress relaxation was within 1–2% of the peak load of a step, in the plastic regime. The applied stresses and measured strains reported are the average values during this data acquisition period. The incident beam was 8 mm high and 4 mm wide, the radial collimators used provided an aperture of 4 mm in the scattered beam. With strain measured in two directions simultaneously on this instrument and with the texture symmetric about the bar axis, only one sample is needed for strain measurements if the compression axis is along the bar axis, to obtain all principal strain directions. However, for compression along the radial direction of the bar, two samples are necessary, one for the case where the measured Poisson strains are along the bar axis and another for the case where the measured Poisson strains are in the radial direction of the bar.

## 3. Experimental results and discussions

### 3.1. Macroscopic mechanical properties

The macroscopic mechanical behaviors of specimen compressed along the bar axial and radial directions are shown in Fig. 3. Two obvious features are observed:

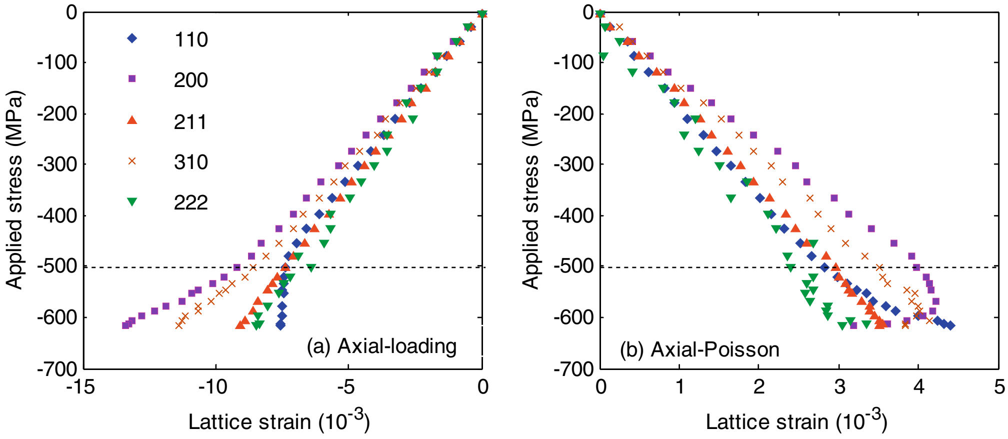

**Fig. 4.** Evolution of lattice strains of individual grain families during compression along the bar axial direction. (a) Responses in the loading direction, (b) responses in the Poisson direction. Dashed line shows the macroscopic yield strength. The errors of the lattice strains are ~10–250 × $10^{-6}$, with the largest errors obtained for the {222} grain family.

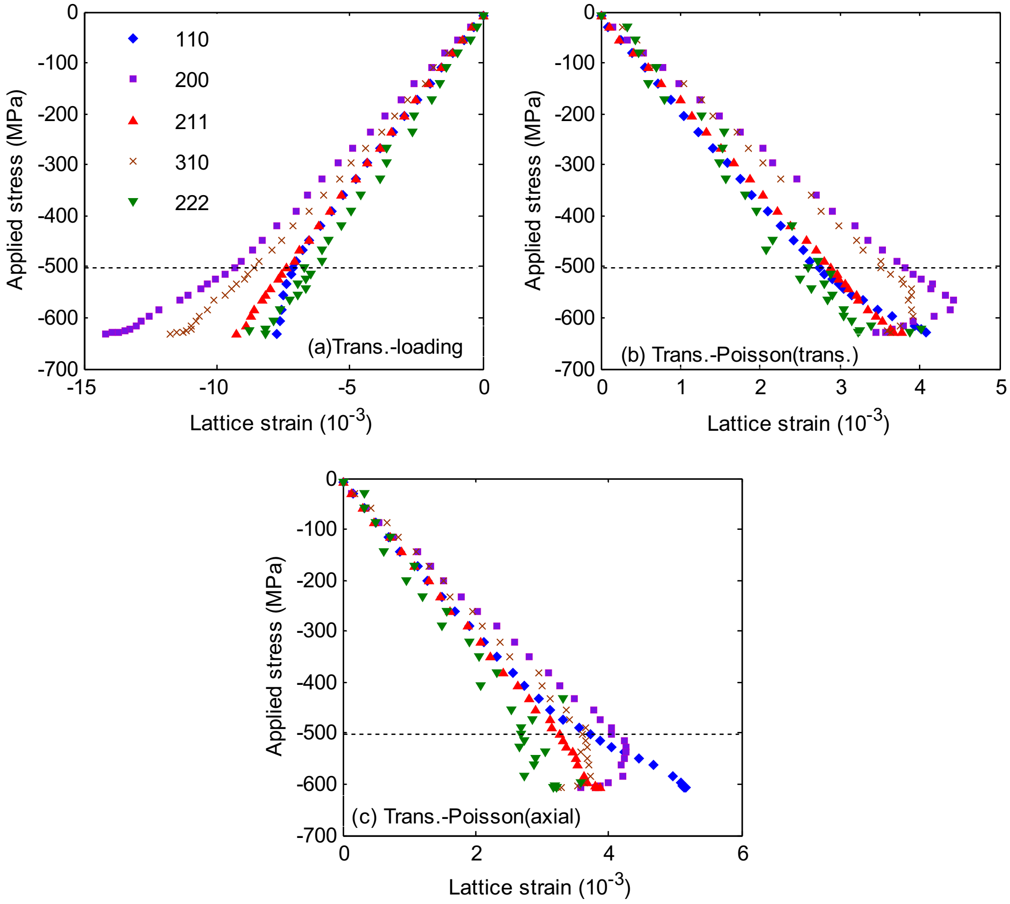

**Fig. 5.** Evolution of lattice strains of individual grain families during compression along the bar transverse direction. (a) Response in the loading direction, (b) responses in the Poisson direction (bar transverse direction) and (c) responses of the second Poisson direction (bar axial direction). Dashed line shows the macroscopic yield strength. The errors of the lattice strains are ~10–260 × $10^{-6}$. The largest errors are obtained in the {222} grain family.

(1) The mechanical responses in both axial and radial directions of the bar are very similar. The measured Young's modulus in the bar axis and bar radial direction is ~60 ± 0.5 GPa, and 58.15 ± 0.9 GPa, respectively. The elastic limit (defined as where the stress strain curve deviates from the linear elastic line) along both bar axis and radial directions is ~500 MPa. The 0.2 offset yield strength is $\sigma_{0.2}$ = ~550 MPa.

(2) At strains larger than 2%, the material exhibits a very low hardening rate and shows almost perfect plasticity.

### 3.2. Evolution of the intergranular strain

The lattice strain evolution for individual grain families, defined as grains having an {hkl} plane lying within 7.5° of the diffraction vector [21], are plotted against the applied true stress in Figs. 4 and 5. For clarity, the responses of only 5 grain families are shown. The measured diffraction elastic moduli of {110}, {200}, {211}, {310}, {222} and {321} grain families compression along the bar axis and radial directions are listed in Table 1. It can be seen that among all the selected grain families, the {222} grain family has the highest elastic modulus, while the {200} grain family has the lowest elastic modulus.

Above an applied stress ~−500 MPa, the lattice strain of the {110} grain family in the load direction increases at a rate lower than the elastic response with increasing applied stress, indicating the yielding of the {110} grain family (Fig. 4(a)), and then the lattice strain quickly reaches a saturation value of ~7500 × $10^{-6}$, meaning that little more stress is taken by {110} grains with increasing applied stress. The yield of the {110} grain family causes load transfer to other grain families, and the lattice strains of the {310} and {200} families increase rapidly relative to their linear elastic response. Compared to the other grain families, the {211} grain family shows little deviation from the elastic response in the plastic region.

In the Poisson direction, the {200} grain family deviates from its linear elastic line and the lattice strains shift back towards compression at an applied stress close to −500 MPa. At the same time,

**Table 1**
Measured diffraction elastic moduli (GPa) of the bulk samples and the individual grain families. P.T. indicates the measurement is made in the Poisson direction, which is the transverse bar direction, P.A. means the measurement is in the Poisson's direction, which is the bar axial direction.

| Sample | Macro- | {110} | {200} | {211} | {220} | {310} | {222} | {321} |
|---|---|---|---|---|---|---|---|---|
| Axial loading | 60.04 ± 0.47 | 64.2 ± 0.1 | 55.5 ± 0.3 | 67.96 ± 0.42 | 64.0 ± 0.42 | 59.1 ± 0.48 | 75.70 ± 3.1 | 67.9 ± 1.05 |
| Axial (P.T.) | | −181.8 ± 2.03 | −120.8 ± 1.46 | −170.2 ± 2.21 | −176.9 ± 2.18 | −140.1 ± 1.83 | −179.7 ± 12.73 | −167.6 ± 6.84 |
| Trans loading | 58.86 ± 0.86 (57.55 ± 0.34) | 67.4 ± 0.19 | 53.6 ± 0.22 | 67.3 ± 0.21 | 67.9 ± 0.54 | 58.9 ± 0.45 | 76.8 ± 2.32 | 69.09 ± 0.75 |
| Trans (P.T.) | | −183.1 ± 1.18 | −129.7 ± 1.19 | −171.0 ± 1.47 | −178.9 ± 3.46 | −140.3 ± 3.58 | −191.0 ± 14.60 | −176.9 ± 5.29 |
| Trans (P.A.) | | −147.9 ± 1.19 | −119.4 ± 1.52 | −151.7 ± 1.50 | −147.4 ± 1.69 | −135.9 ± 2.03 | −172.9 ± 9.80 | −66.4 ± 6.04 |

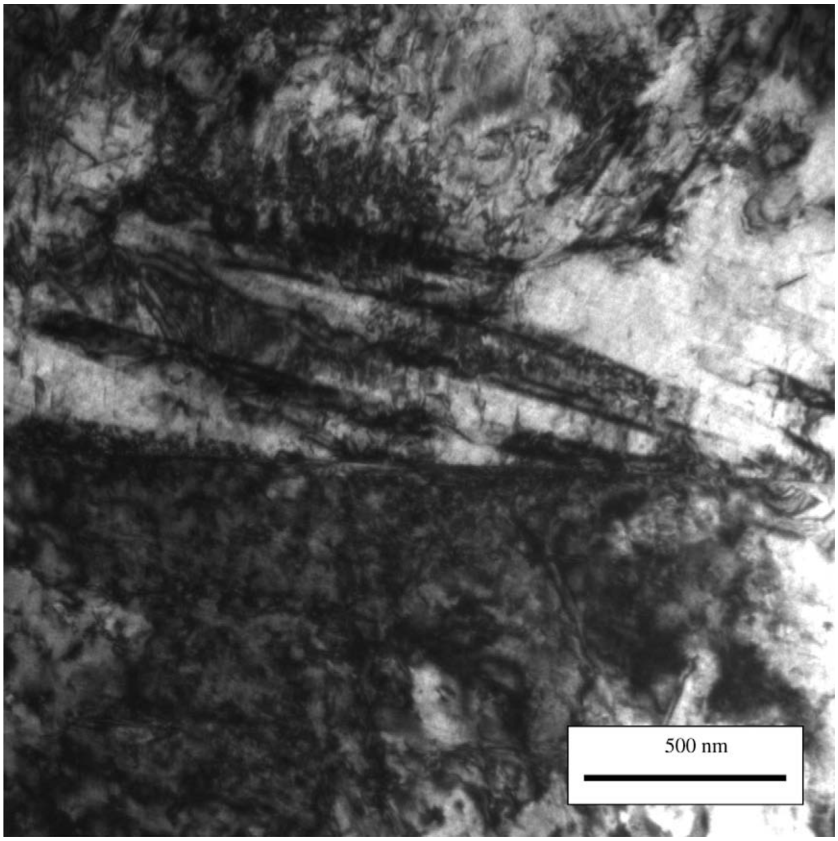

**Fig. 6.** TEM image of material after deformation showing twins, which were identified as {112}⟨1 1 1⟩.

the strain of the {110} grain family shifts towards more tensile strains. At an applied stress close to −600 MPa, a sharp 'kick back' in strain is observed for the {200} and {310} grain families. The evolution of the lattice strain of the {211} family approximates to a straight line during deformation.

Compression along the radial direction of the bar results in evolution of lattice strains in the elastic and plastic regions in the loading direction similar to that for compression along the bar axis (Fig. 5(a)). However, the two Poisson's directions behave very differently during compression along the radial direction; in the bar radial direction, the Poisson lattice strains of {110}, {200} and {310} grain families do not show inflections until the applied stress is close to −600 MPa (Fig. 5(b)). Along the bar axis, the Poisson lattice strains of these grain families deviate from the linear elastic relation much earlier at an applied stress of ~500 MPa (Fig. 5(c)). The elastic anisotropy in the axial direction of the bar is smaller than that in the radial direction.

EBSD studies of the deformed material showed no evidence of twins in samples studied after deformation. However, on TEM examination, some very fine {112}⟨1 1 1⟩ twins were seen (Fig. 6).

### 3.3. Discussion

Due to the weak texture, the macroscopic mechanical responses are very close in the bar axial and radial directions. The measured Young's modulus is about 60 GPa, which is much smaller than that of α-Zr. It is noted that the compression test is very sensitive to the sample alignment; therefore, the value of macroscopic Young's modulus determined by clip gauge potentially has a large uncertainty. The macroscopic strength of this β-phase material compares well with the flow stress of 550 MPa reported in [12] for Zr–20%Nb, which had O ~630 wppm and grain size ~100 μm. Thus any reduced Hall–Petch hardening [22] due to the larger grain size of our material is probably offset by its higher O content. The high strength observed in the β-phase thus likely results from the solution strengthening effects of the O and Nb alloying elements [12,23]. Precipitation strengthening due to the presence of any ω-phase [6] is possible but unlikely to be significant, due to (a) the small volume fraction of ω-phase present and (b) the precipitates are small and coherent, hence being easily cut. Compared to *bcc* iron [24–26], $\beta_{Zr}$ has a very low hardening rate when the deformation strain is larger than 2%. The reason for the low hardening rate is not known but may be due to dynamic recovery caused by cross-slip as proposed for *bcc* Mo [27].

The small number of twins found suggest that dislocation slip is the major deformation mode of this material, which is somewhat consistent with the study reported in [12], where {332}⟨1 1 3⟩ twinning was found in quenched Zr–13.5%Nb but only slip was observed in quenched 19%Zr to 22%Nb alloys. However in [12], {112}⟨1 1 1⟩ twins were only observed in Zr–Nb alloys with greater than 40%Nb. A number of potential reasons exist for the differences between this observation and our own including; (1) the material in [12] had a lower O content (630 wppm c.f. 1360 wppm in this study); (2) the alloys in the 13–40%Nb composition range that were studied in [12] were observed to have a 'Widmanstatten' plate microstructure (presumably showing remnant α-phase, though not identified crystallographically as such in Ref. [12]) – it is interesting, though perhaps coincidental, that the composition range in [12] where no {112}⟨1 1 1⟩ twins were observed was also the range in which the initial 'Widmanstatten' plate microstructure was found. Nonetheless, we can assume that pencil glide deformation along ⟨1 1 1⟩, plays the major role in deformation of this quenched $\beta_{Zr}$ with some contribution from {112}⟨1 1 1⟩ twinning.

In a cubic crystal, the stiffness of a given grain family {hkl} in the loading direction depends on their elastic anisotropy factors $A_{hkl} = (h^2k^2 + k^2l^2 + l^2h^2)/(h^2 + k^2 + l^2)$ [28]. Thus, the stiffness of the selected grain families is expected to increase in the order {200}, {310}, {110} and {111} for most metals. This trend is clearly seen in Figs. 4 and 5 in both the loading and the Poisson's directions. Compared to the α-phase, whose crystal moduli range from ~90 to 125 GPa, the elastic moduli of the β-phase are very low. Since *bcc* β-phase is less densely packed compared to *hcp* α-phase, this might be typical for materials that undergo an *hcp* to *bcc* phase transformation, since similar results have been observed in Ti alloys [29].

Due to the elastic anisotropy, the interaction among the different grain families in the elastic region causes the {110} grain family to bear more load and yield at a lower applied stress even though it is among the least favorably orientated for slip (i.e., the largest Taylor factor) [18]. The {222} grain family is even stiffer than the {110} family (see Table 1) and it has the same Taylor factor as the {110} grain family [30], thus it is expected to bear more load and yield first among all the grain families. However, this is not clearly seen in Figs. 4 and 5. This may be attributed to the poor data quality due to the very low peak intensity. It is also possible that the post yielding load transfer from the {222} family to other grain families is very quick, which obscures the inflection of the {222} curve. The effect of elastic anisotropy on the plasticity in cubic polycrystals has been discussed in [24].

Compared to *bcc* iron [24], the intergranular strain distribution in the loading direction is larger in the *bcc* $\beta_{Zr}$ at a given plastic strain. This is due to the low work hardening rate of the {110} grain family. In Fe [24], the lattice strain of the {110} orientation kept increasing with the applied stress in the plastic region, while in this $\beta_{Zr}$, as shown in Figs. 4(a) and 5(a), little more stress is taken by the {110} grain family once it yields. The load increment is then shared by the other grain families. Consequently, the lattice strains of other grains increased at a larger rate and resulted in larger intergranular strains than that seen in iron [24]. The low work hardening for the {110} grain family is possibly due to dynamic recovery as proposed for *bcc* Mo [27], and mentioned before. Another possible reason might relate to the finding of Arsenault and Law [31], in their study on single crystal Ta and Ta based alloys. Arsenault and Lawley found that increasing solute concentration (both interstitial and substitutional) eliminated or reduced the work hardening rate in the stage II single crystal deformation. They attributed this to the fact that dislocation slip was limited to the primary slip system by solute atoms and a large latent hardening of the primary slip system on secondary slip systems. In polycrystals, it nominally requires five independent slip systems for an arbitrary shape change. Hence the complete elimination of secondary slip systems seems unlikely. However, if the activity of the secondary slip is reduced by solute element or primary slip and hence reduces the possibility of dislocation interactions between slip systems (i.e. reduced forest hardening), a low work hardening rate is still reasonable.

In the Poisson direction, the internal strains developed in the elastic region were cancelled by the strain 'kick back' of the {200} and {310} grain families, which resulted in a small final intergranular strain in the Poisson direction on unload. However, the strain evolution in this $\beta_{Zr}$, especially the 'kick back' of the {200} and {310} orientations in the Poisson's direction, is very similar to that observed in single phase iron [24] and iron in a dual phase material [20]. The reason for the sharp strain 'kick back' of {200} and {310} grain families in the Poisson's directions has been discussed in [24,32]. In a *bcc* crystal, the distribution of slip directions does not facilitate uniform contraction or expansion in the Poisson's directions in some grains (e.g. for {200} grains with the ⟨2 0 0⟩ in the Poisson direction and the ⟨1 1 0⟩ aligned in the loading direction). During compression, this non-uniform expansion causes large transverse incompatibilities between these grain families and the surrounding medium, which must be accommodated by large compressive strains in these grains. A rapid strain shift back towards compression is thus seen. Since a {hkl} grain family in the Poisson's direction includes grains that belong to many of the axial grain families – as long as they have a common ⟨h k l⟩ direction pointing towards the Poisson direction – strains of a {hkl} Poisson grain family are very sensitive to the texture. A detailed description and discussion of these effects can be found in [24].

The small intergranular strain accumulated in the {211} grain family during plasticity suggests that it might be a good candidate for representing the average phase behavior for $\beta_{Zr}$ for studies of dual phase materials when the effect of $\beta_{Zr}$ is in consideration. More discussion of this is given in Section 6.

## 4. Modeling method

Elasto-Plastic Self-Consistent (EPSC) models simulate the interaction among different grain orientations during deformation by accounting for both the strain compatibility and stress equilibrium. Since the early implementation by Hutchinson [33], EPSC models have been widely used to describe the elasto-plastic properties of polycrystalline aggregates and have been shown to give good simulations of the deformation behavior of single phase materials [34,35], with particular success in describing the deformation of cubic materials [24,25]. In this paper, the EPSC of Turner et al. [34,35] is used to interpret the deformation behavior of single phase $\beta_{Zr}$ and to estimate the elastic and plastic properties.

In the EPSC model, a population of grains is selected with a distribution of orientations and volume fractions determined from the measured texture. Each grain, which has the anisotropic elastic constants and plastic deformation characteristics of a single crystal of the material under study, is treated as an ellipsoidal inclusion embedded in a Homogenous Effective Medium (HEM) that has the average properties of all grains. Interactions between individual grains and the HEM are treated using an Eshelby tensor [33]. No lattice rotation or texture evolution is considered in this model and thus it is valid only for small strain deformation. More details can be found in [36].

Using EPSC, the single crystal elastic constants $C_{ij}$ can be determined from the polycrystalline data based on the measured texture and the diffraction elastic constants [37]. In this method, elastic constants $C_{ij}$ are estimated first, then EPSC is run in the elastic region by applying a small amount of strain and the calculated macroscopic Young's modulus and the diffraction elastic constants of each individual grain family are compared to the experimental results. In our case, the experimental constants of the {110}, {200}, {211}, {220}, {310}, {222} and {321} were compared for the stress applied in the bar radial direction, with simultaneous fit to all three data sets (axial and both Poisson directions). An iterative least squares approach was used to obtain values of $C_{ij}$. The determined crystal elastic constants for $\beta_{Zr}$ at room temperature are $C_{11} = 145.9 \pm 2.6$ GPa, $C_{12} = 117.4 \pm 2.5$ GPa and $C_{44} = 29.8 \pm 0.2$ GPa.

In the plastic region, as discussed above, twinning is not the major deformation mode in this material and plastic deformation is caused mostly by dislocation slip. The typical deformation mode for *bcc* crystals is pencil glide, where dislocations slip on many slip planes with the ⟨1 1 1⟩ slip direction in common. In order to simplify the model, three slip systems are normally considered during simulation, namely the {110}⟨1 1 1⟩, {112}⟨1 1 1⟩ and {123}⟨1 1 1⟩ [38]. The total number of the potential slip systems is 96.

**Table 2**
Parameters used in EPSC model.

| Slip system | $\tau_0$ (GPa) | $\tau_1$ (GPa) | $\theta_0$ | $\theta_1$ |
|---|---|---|---|---|
| {110}⟨1 1 1⟩ | 0.235 | 0.01 | 1 | 0.001 |
| {112}⟨1 1 1⟩ | 0.235 | 0.01 | 1 | 0.001 |
| {123}⟨1 1 1⟩ | 0.235 | 0.01 | 1 | 0.001 |

The hardening of each slip system is described by an extended Voce law [39]

$$\tau^s = \tau_0^s + (\tau_1^s + \theta_1^s \Gamma)\left(1 - \exp - \left(\frac{\theta_0^s \Gamma}{\tau_1^s}\right)\right), \tag{1}$$

where $\tau_0^s$ is the threshold value, $\tau_1^s$ is the Voce stress where the hardening extrapolates to zero, $\theta_0^s$ is the initial hardening rate and $\theta_1^s$ is the final asymptotic hardening rate for the slip system $S$, $\Gamma$ is the accumulated shear strain in the grain. Twinning is not included in the model.

Taking into account the 'self' and 'latent' hardening, the increment of the threshold stress of a slip system due to shear activity in a grain is calculated by [36]:

$$\Delta\tau^s = \frac{d\tau^s}{d\Gamma} \sum_{s'} h^{ss'} \Delta\gamma^{s'}, \tag{2}$$

where $h^{ss'}$ represents the obstacles that the shear of dislocation '$s'$', '$\Delta\gamma^{s'}$', causes for the propagation of dislocation '$s$'. Parameters in Eqs. (1) and (2) were unknown initially and were determined by iterative comparisons between the experimental results and the modeling simulations. We assume an isotropic hardening, i.e. the latent hardening and the self hardening are the same. A total number of 1944 gains were used in the EPSC model. The CRSS and hardening parameters of each slip mode, which give the best simulations, are listed in Table 2. The same parameters are used for the three slip systems as further variation did not generate significant improvement in modeling results. Also it has been proposed by Hutchinson [40] that if the number of slip planes is large enough and they are well distributed about the slip direction, then the model is insensitive to the planes explicitly specified. Using the same parameters for all three slip systems in modeling has been adopted by e.g. Chin and Mammel [30] and others [20,25].

## 5. Comparison between experimental and modeling results

The modeled macroscopic mechanical properties are compared to the experimental results in Fig. 3. It is seen that using parameters listed in Table 2, the EPSC model almost perfectly described the macroscopic mechanical behavior of this material. It accurately reproduced the Young's modulus and the yield strength. The stress strain characteristics such as: the very low hardening rate and the small texture effects on strength were also well captured.

The comparison between the calculated lattice strain evolution and the experimental results is plotted in Figs. 7 and 8. In the elastic region, the EPSC model quantitatively calculated the diffraction elastic constant of all the selected grain families in both the loading and the Poisson directions. The method described in the previous section is an effective way to determine the single crystal elastic constants from the polycrystalline data, thus the elastic constants of the $\beta_{Zr}$ given above are considered reasonably reliable and can be used in the future studies of ZrNb alloys. To the authors' knowledge, this is the first time single crystal elastic moduli for $\beta_{Zr}$ have been reported. Based on the obtained elastic constants, the calculated Young's modulus for ⟨2 0 0⟩, ⟨3 1 0⟩, ⟨1 1 0⟩, ⟨2 1 1⟩ and ⟨1 1 1⟩ directions is ~41.2, 47.7, 66.2, 66.2 and 82.9 GPa, respectively. The calculated Young's moduli of the bulk material in the bar axial and radial directions are both ~63 GPa, which are close to the measured values.

In the early part of the plastic region, EPSC quantitatively predicted the yielding of all the selected grain families in both the loading and the Poisson directions, and qualitatively described the interaction among these individual orientations. Features like the load transfer and the sharp 'kick back' of the {200} and {310} in the Poisson directions were well captured. In Figs. 7 and 8, it can be seen that the modeled {200} and {310} grain families yielded a little earlier than was shown by the experiments, implying that the calculated Young's moduli of these two grain families might be slightly higher than the real values. As discussed in [24], the Poisson strain in the elastic region is very sensitive to the texture. The elastic constants reported in Section 4 are obtained by fitting the measured diffraction elastic moduli in all the loading and Poisson's directions. Since the results of the two Poisson's directions weight more than that of the loading direction in the least square routine, a small error of texture measurement or misalignment of sample will generate uncertainties in the calculated elastic constants even though they give the best overall agreement to the measured data.

The EPSC model failed in simulating the lack of hardening observed in the {110} orientation with increasing deformation strain. The calculated lattice strain increases slowly with increasing stress, while the experiment shows a constant lattice value, which indicates that no more stress is taken by the {110} orientation. To balance the calculated strong {110} response, the modeled {310} and {200} orientations are softer than indicated by the experimental results. This causes the calculated intergranular strain in the loading direction to be smaller than the experimental data suggest.

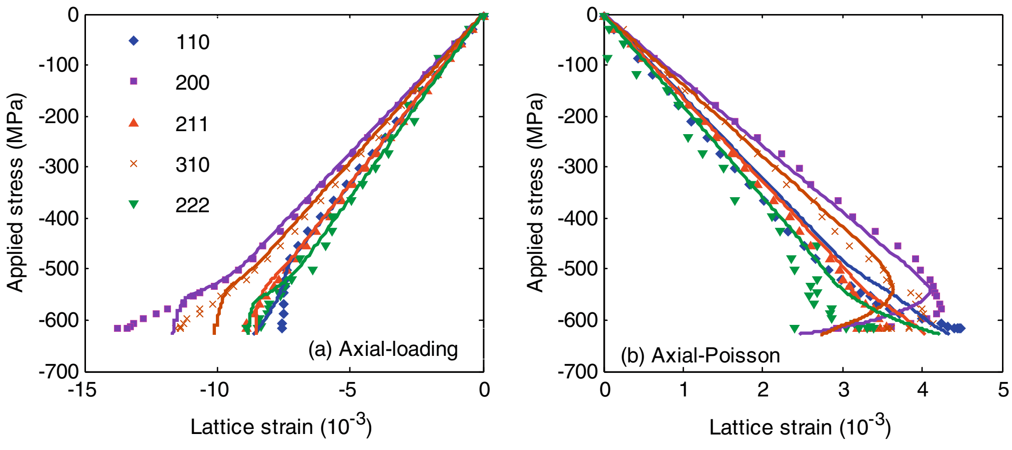

**Fig. 7.** Comparison between the EPSC model (lines) and the experimental results (dots) for the axial sample: (a) loading direction and (b) Poisson's direction.

In order to test if a large latent hardening of the primary slip can limit the activity of the secondary slip and results in a low work hardening rate as mentioned previously, the latent hardening (i.e. $h^{ss'}$ in Eq. (2) where $s \neq s'$) in the EPSC model was increased by a factor of 100 aiming to limit the occurrence of secondary slip. The results are plotted in Fig. 9. A large work hardening rate was obtained, indicating that, as expected, no matter how big the latent hardening, secondary slip has to occur to meet the strain compatibility and thus generate a large overall hardening rate in grains. It is not very clear why the EPSC model failed to capture the soft {110} behavior even the hardening parameters are very small. In the EPSC model, for a system to slip, the stress must be and remain on the yield surface during each incremental step. To do that, once the resolved shear stress, $\tau^{s,c}$ of a certain slip system in a grain,

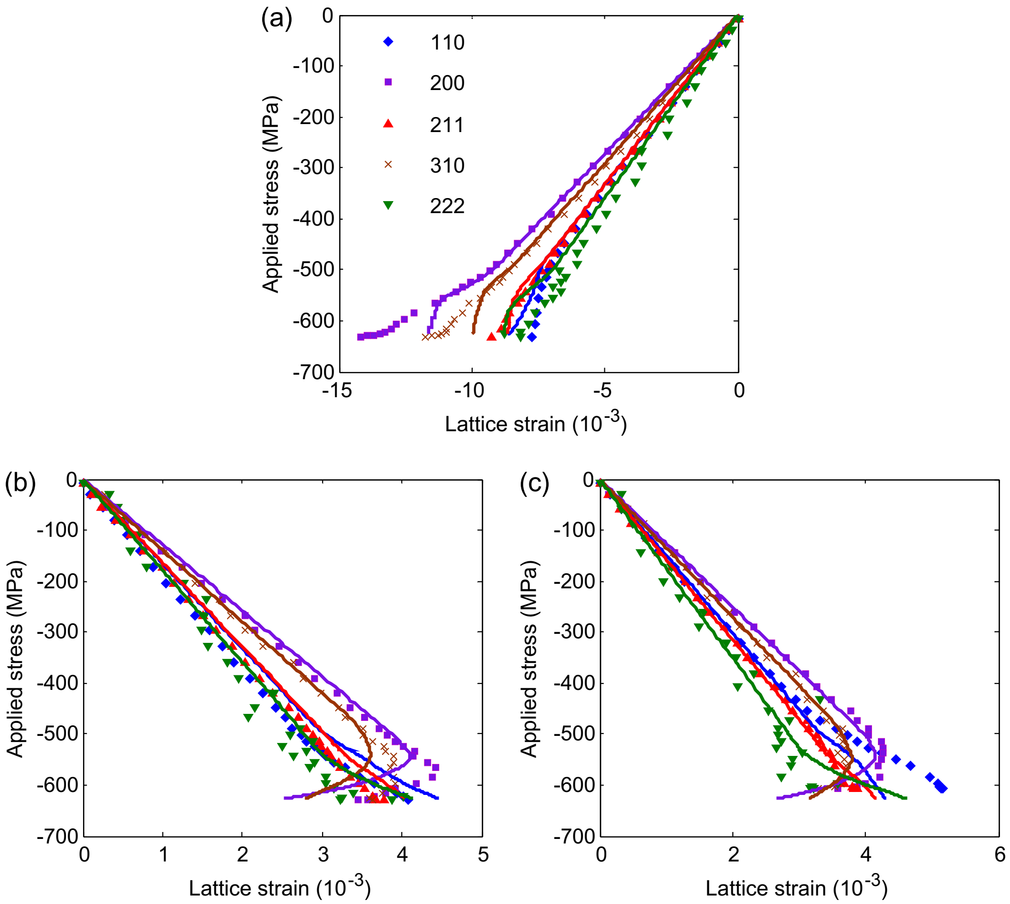

**Fig. 8.** Comparison between the EPSC model and the experimental results for the transverse sample: (a) loading direction, (b) Poisson's direction (bar radial direction) and (c) Poisson's direction (bar axial direction).

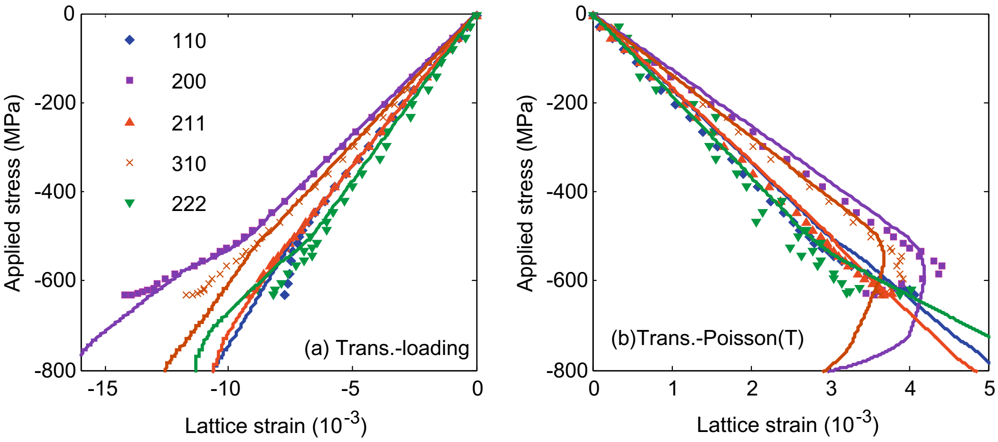

**Fig. 9.** Comparison between the EPSC model and the experimental data, {110}⟨111⟩ slip, $\tau_0 = 0.22$, $\tau_1 = 0.001$, $\theta_0 = 1$ and $\theta_1 = 0.0001$, self hardening = 0.1 and latent hardening = 100.

which depends on the properties of the HEM, exceeds the critical shear stress ($\tau^s$), $\tau^s$ is then increased to the value of the $\tau^{s,c}$ instead of altering the stress state [36]. This scheme prevents a slip system from exhibiting behavior that is too soft no matter how small the hardening rate for that system. However, it may not be true under real situations. Also, we should realize that the simple hardening functions (i.e. Eqs. (1) and (2)) are not sufficient for the complicated dislocation evolution during deformation such as dynamic recovery caused by cross-slip or dislocation rearrangement.

## 6. Determination of the average phase behavior

For a multiphase material, it is important to understand the contribution of each phase to the average properties. However, a quantitative simulation of the interaction among phases and thus the corresponding interphase stresses during deformation still remains challenging. Part of the reason is the difficulty in determining the average phase behaviors experimentally. Two different neutron diffraction techniques are currently employed for this purpose based on the characteristics of the beam used. At reactor sources, where a monochromatic neutron beam is used, diffraction of individual peaks is measured separately. It is time consuming and not practicable to measure many diffraction peaks and most of the time only diffraction from a limited number of peaks can be measured. Thus the average phase stress–strain behavior is normally taken to be that of those grain families in the phase whose applied stress vs. lattice strain curves remain more or less linear even when plasticity is extensive (i.e. those which exhibit small intergranular strains) [41–44], such as (10–10) for Ti [42] and (311) for *fcc* iron [43] and (110) for *bcc* iron [44]. However, there is no absolute choice for a suitable plane for the average phase strain. Different workers have selected different planes for the same phase in the past depending on experimental conditions and materials. At a Time Of Flight (TOF) source, where a pulsed white neutron beam is used, it is common practice to define the average phase strains using a multiphase Rietveld refinement by making a least squares fit between the observed and predicted results [45,46]. Rietveld refinement produces a very good fit at the zero load condition. However, as load increases, larger errors are expected caused by the elastic and plastic anisotropy which are not included in this method at the current stage. Clearly, an accurate method would account for the strains of all the grain families and average them by weight as indicated in [47], but this is difficult if the texture changes during deformation.

To facilitate the future study of deformation mechanisms of Zr–Nb dual phase alloys, it is worth investigating which method gives a more accurate estimation of the average elastic strain of the β-phase. The results of the three methods, i.e. the single peak, Rietveld fitting and the peak average, are compared to the measured macroscopic elastic properties in Fig. 10(a) and are summarized as below:

(1) Among all the diffraction peaks, the lattice stress strain curve of the {211} orientation remained near linear in the whole deformation range. Its diffraction elastic constant is ~67 GPa, which is slightly higher than the macroscopic Young's modulus ~60 GPa, However, in cases where only very limited diffraction peaks can be monitored at a reactor source, the {211} orientation is a good candidate in representing the average phase behavior for $\beta_{Zr}$ with a similar texture.

(2) It is shown that the Rietveld methods works well in the elastic region but follows the trace of the {110} orientation and shows stress relaxation in the plastic regime. Fig. 10(b) shows that at the high stress level, with increasing internal stresses, as expected, a single lattice parameter is not sufficient to fit all the diffraction peaks [20]. From Fig. 10(b), it can be seen that the strong {110} intensity gives {110} grain family a higher weight during the refinement, and the lattice parameter is then tuned to give a good fit to the {110} diffraction by sacrificing the others (e.g. {200}). The Rietveld method is thus not ideal for a $\beta_{Zr}$ material with a similar extrusion texture, and would be used as a best approximation only where required due to poor counting statistics. It should also be noted that the {110}, {200} and {211} $\beta_{Zr}$ peaks overlap with the ω-phase {201}, {300} and {110} peaks [16]. This will be a minor influence on the quality of the fit, given the quantity of ω-phase present.

(3) The peak average calculated using the method B proposed in [47] based on the responses of the {110}, {200}, {211}, {310}, {222} and {321} orientations show a near linear relationship during the whole deformation range. The calculated elastic modulus is ~64 GPa, which is close to the macroscopic elastic constant. Clearly, the peak average is the best choice for estimation of the average phase response in the multiphase materials once the responses of many peaks are available.

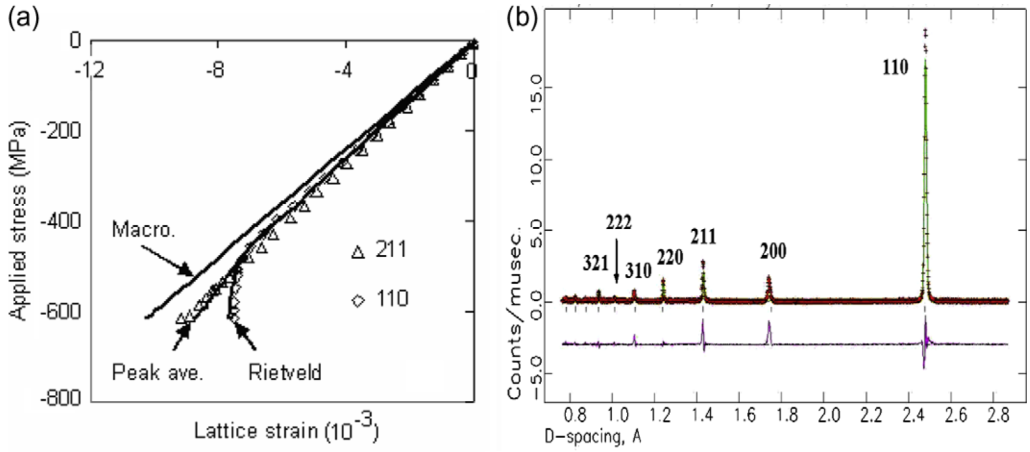

**Fig. 10.** (a) Comparison of the phase response obtained by different methods. (b) Rietveld refinement at stress ~615 MPa. The first line shows the TOF diffraction spectrum, the black dots below each peak indicate the predicated peak position. The second shows the residual of the Rietveld fitting.

## 7. Summary

Room temperature elastic and plastic properties of the $\beta_{Zr}$ with 20 wt%Nb have been studied using neutron diffraction compression experiments. Following conclusions are drawn:

(1) The β- to α+β-phase transformation temperature of this material was found to be ~800 °C, in agreement with [16,48].
(2) The measured bulk Young's modulus is ~60 GPa, which is lower than that of $\alpha_{Zr}$, while the yield strength is ~500 MPa. The high yield strength is probably related to solution strengthening from the O and Nb alloying elements, as well as possible minor precipitation strengthening contributions from the ω-phase.
(3) Some {112}⟨1 1 1⟩ twins can be found by TEM after 10% deformation, but dislocation slip is considered the major mode for plasticity.
(4) The EPSC model is used to interpret the experimental results and is shown to be effective in extracting the single crystal properties from the polycrystalline data as well as in modeling the early part of the plastic deformation. The calculated single crystal elastic constants of $\beta_{Zr}$ with 20 wt%Nb at room temperature are: $C_{11}$ = 145.9 ± 2.6 GPa, $C_{12}$ = 117.4 ± 2.5 GPa and $C_{44}$ = 29.8 ± 0.2 GPa. The calculated Young's modulus of ⟨1 0 0⟩, ⟨1 1 0⟩, ⟨1 1 1⟩, ⟨2 1 1⟩ and ⟨3 1 0⟩ directions is ~41.2, 66.2, 82.9, 66.2 and 47.7 GPa, respectively. The modeled Young's modulus is about 63 GPa. The fitted CRSS for slip on {110}, {112} and {123} planes are the same and have a value of 235 MPa.
(5) Among the three methods for describing the average phase behavior, i.e. single peak, the Rietveld refinement and the peak average, the peak average gives the best description. In cases where only a limited number of diffraction peaks available, {211} orientation still closely represents the average phase response for a $\beta_{Zr}$ material with a similar extrusion texture.

## Acknowledgements

The authors would like to thank Dr M.A. Gharghouri for the texture measurement and Dr I. Yakobtsov for the EBSD observations. This work is sponsored by NSERC, COG, OPG and Nu-Tech Precision Metals under the Industrial Research Chair Program in Nuclear Materials at Queen's University. Texture was measured at the National Research Universal (NRU) reactor at the AECL Chalk River Laboratory (CRL), Canada. The compression tests were carried out at ISIS pulsed neutron facility, Rutherford Appleton Laboratory, UK.

## References

[1] D.G. Hurst, Canada Enters the Nuclear Age, McGill-Queen's University, 1997.
[2] R.A. Holt, J. Nucl. Mater. 372 (2008) 182.
[3] K. Moriii, H. Mecking, G. Lűtjering, in: H.J. McQueen et al. (Eds.), Proceedings 7th International Conference on Strength of Metals and Alloys, Pergamon, Oxford, 1985, p. 251.
[4] A. Jaworski Jr., S. Ankem, Metall. Mater. Trans. 37A (2006) 2739.
[5] B.A. Cheadle, C.E. Ells, J. Electrochem. Technol. 4 (1966) 329.
[6] B.A. Cheadle, S.A. Aldridge, J. Nucl. Mater. 47 (1973) 255.
[7] S. Kim, Metall. Mater. Trans. 37A (2006) 59.
[8] N. Christodoulou, P.A. Turner, C.N. Tome, C.K. Chow, R.J. Klassen, Metall. Mater. Trans. A 33 (2002) 1103.
[9] C.N. Tome, N. Christodoulou, Philos. Mag. 80 (2000) 1407.
[10] M.K. Kumar, I. Samajdar, N. Venkatramani, G.K. Dey, R. Tewari, D. Srivastava, S. Banerjee, Acta Mater. 51 (2003) 625.
[11] S. Cai, M.R. Daymond, R.A. Holt, E.C. Oliver, Adv. Mater. Res. 15–17 (2007) 615.
[12] K. Nishimura, S. Hanada, O. Izumi, J. Mater. Sci. 25 (1B) (1990) 384.
[13] S. Hanada, T. Yoshio, O. Izumi, J. Mater. Sci. 21 (3) (1986) 866.
[14] C.E. Liundin, R.H. Cox, USAEC Report GEAP-4089, vol. 1, 1962, p. 9.
[15] G. Lntjering, J.C. Williams, Titanium, Springer-Verlag, 2003.
[16] C.W. Dawson, S.L. Sass, Metall. Trans. 1 (8) (1970) 2225.
[17] U.F. Kocks, C.N. Tomé, H.R. Wenk, Texture and Anisotropy, Cambridge University, 1998.
[18] W.F. Hosford, The Mechanics of Crystals and Textured Polycrystals, Oxford University, New York, 1993.
[19] E.A. Calnan, C.J.B. Clews, Phil. Mag. 42 (1951) 616.
[20] M.R. Daymond, H.G. Priesmeyer, Acta Mater. 50 (2002) 1613.
[21] J.R. Santisteban, M.R. Daymond, L. Edwards, J.A. James, J. Appl. Cryst. 39 (2006) 812.
[22] D. Hull, Acta Metall. Mater. 9 (1961) 191.
[23] O. Ruano, G. Elssner, J. Less–Common Met. 52 (1977) 153.
[24] E.C. Oliver, M.R. Daymond, P.J. Withers, Acta Mater. 52 (2004) 1937.
[25] J.W.L. Pang, T.M. Holden, T.E. Mason, J. Strain Anal. 5 (1998) 373.
[26] Y. Tomota, P. Lukas, S. Harjo, J.-H. Park, N. Tsuchida, D. Neov, Acta Mater. 51 (2003) 819.
[27] C. Turk, E. Scala, in: J.P. Hirth, J. Weertman (Eds.), Work Hardening, Gordon and Breach Science Publishers, New York, 1968, p. 333.
[28] J.F. Nye, Physical Properties of Crystals, Oxford University, 1985.
[29] S. Ankem, H. Margolin, Metall. Trans. 11A (1980) 963.
[30] C.Y. Chin, W.L. Mammel, Trans. TMS–AIME 239 (1967) 1400.
[31] R.J. Arsenault, A. Lawley, in: J.P. Hirth, J. Weertman (Eds.), Work Hardening, Gordon and Breach Science Publishers, New York, 1968, p. 283.
[32] E.C. Oliver, PhD thesis, University of Manchester, 2002.
[33] J. Hutchinson, J. Proc. R. Soc. 319 (1970) 247.
[34] P.A. Turner, N. Christodoulou, C.N. Tomé, Int. J. Plasticity 11 (1995) 251.
[35] P.A. Turner, C.N. Tomé, Acta Metall. Mater. 42 (1994) 4143.
[36] C.N. Tomé, E.C. Oliver, Code: Elasto-Plastic Self-Consistent (EPSC), Version 3, 2002.
[37] B. Clausen, S.Y. Lee, E. Űstündag, C.P. Kim, D.W. Brown, M.A.M. Bourke, Scripta Mater. 54 (2006) 343.
[38] M.R. Daymond, C. Hartig, H. Mecking, Acta Mater. 53 (2005) 2805.
[39] C. Tome, G.R. Canova, U.F. Kocks, N. Christodoulou, J.J. Jonas, Acta Metall. 32 (1984) 1637.
[40] J.W. Hutchinson, J. Mech. Phys. Solids 12 (1964) 25.
[41] J.W.L. Pang, T.M. Holden, P.A. Turner, T.E. Mason, Acta Mater. 47 (1999) 373.
[42] P.J. Withers, A.P. Clarke, Acta Mater. 46 (1998) 6585.
[43] M.R. Daymond, C.N. Tome, M.A.M. Bourke, Acta Mater. 48 (2000) 553.
[44] A. Baczmański, C. Braham, Acta Mater. 52 (2004) 1133.
[45] M.R. Daymond, M.A.M. Bourke, R.B. Von Dreele, B. Clausen, T. Lorentzen, J. Appl. Phys. 82 (1997) 1554.
[46] M.R. Daymond, M.A.M. Bourke, R.B. Von Dreele, J. Appl. Phys. 85 (1999) 739.
[47] M.R. Daymond, J. Appl. Phys. 96 (2004) 4263.
[48] H. Richter, P. Wincierz, K. Anderko, U. Zwicker, J. Less–Common Met. 4 (3) (1962) 252.